

Shape-induced pairing of spheroidal squirmers

Ruben Poehnl¹ and William E. Usual^{1,*}

¹*Department of Mechanical Engineering, University of Hawai'i at Mānoa,
2540 Dole Street, Holmes Hall 302, Honolulu, Hawaii 96822, USA*

(Dated: October 31, 2023)

The “squirmers model” is a classical hydrodynamic model for the motion of interfacially-driven microswimmers, such as self-phoretic colloids or volvocine green algae. To date, most studies using the squirmers model have considered spherical particles with axisymmetric distribution of surface slip. Here, we develop a general approach to the pairing and scattering dynamics of two spheroidal squirmers. We assume that the direction of motion of the squirmers is restricted to a plane, which is approximately realized in many experimental systems. In the framework of an analytically tractable kinetic model, we predict that, for identical squirmers, an immotile “head-to-head” configuration is stable only when the particles have oblate shape and a non-axisymmetric distribution of surface slip. We also obtain conditions for stability of a motile “head-to-tail” configuration: for instance, the two particles must have unequal self-propulsion velocities. Our analytical predictions are compared against detailed numerical calculations obtained using the boundary element method.

INTRODUCTION

Self-assembly [1–4], clustering [5–9], and particle motility alignment [10–14] are among the most discussed topics in the active matter community. In each of these phenomena, collective behavior emerges from non-equilibrium interactions between self-motile microscopic particles. These particles usually self-propel through liquid, making hydrodynamic interactions – interactions mediated by flow in the suspending medium – an important and ubiquitous non-equilibrium effect [15].

A broad class of synthetic and biological microswimmers propel themselves by driving flow within a thin layer at the fluid/solid interface. For instance, ciliated microorganisms are covered by a thin carpet of thread-like appendages that beat in a coordinated fashion. The squirmers model, first introduced by Lighthill [16] and Blake [17], was originally developed to describe the motion of ciliated, spherical micro-organisms [18]. In the simplest version of this model, the detailed, time-dependent motion of the cilia is coarse-grained as a prescribed steady tangential slip velocity. This slip velocity provides the interfacial actuation (*i.e.*, thrust) needed for self-propulsion. Additionally, the slip velocity drives flow in the surrounding solution, leading to long-ranged hydrodynamic interactions between the squirmers and other objects in the solution. These features have made the squirmers model a popular approach for understanding the flow-mediated interactions between swimming microorganisms, as well as between microorganisms and bounding surfaces [19–25]. For instance, Ishikawa *et al.* exhaustively cataloged the collision and scattering dynamics of squirmers pairs [19]. As another example, various studies have addressed nutrient uptake (*i.e.*, feeding) of microorganisms in the framework of the squirmers model [26, 27].

Since its original development, the squirmers model has found applications well beyond its initial purpose. For in-

stance, synthetic active colloids driven by self-generated gradients of a thermodynamic variable (*e.g.*, temperature, chemical potential, or electrical potential [28–31]) can often be approximated as “effective squirmers.” Instead of resolving the propulsion mechanism in detail, a slip velocity on the surface of the particle is prescribed [32]. The slip determines two major swimming properties, speed U_s and stresslet \mathbf{S} [33, 34]. As an example that justifies this approach, it was recently observed that metallo-dielectric Janus discoids, energized by AC fields, tend to form “head-to-head” bound pairs [35]. Modeling of the propulsion mechanism (induced charge electrophoresis [36, 37]) revealed that hydrodynamic interactions dominated interactions between particles, *i.e.*, the particles behaved as effective squirmers.

One microscopic property that has proven to be important in active matter is particle geometry [38–41]. Shape can impact the swimming speed of an active particle, the rate of working, and the flow field sourced by the particle [42–47]. Collisions between rod-like particles can lead to nematic ordering in an active suspension [48]. In view of the importance of shape, various studies have considered non-spherical squirmers – usually prolate spheroids [23, 42, 49, 50]. For instance, Ishikawa and Hoto modeled the paramecium *P. caudatum* with a prolate spheroid actuated by interfacial slip. The slip was assumed to be a superposition of five harmonic functions of the elevation angle [51]. In an effort to fully generalize the squirmers model to both prolate and oblate spheroids, we recently developed and characterized a complete set of orthogonal, axisymmetric squirming modes in spheroidal coordinates [52]. We found that the odd-numbered squirming modes contribute to the self-propulsion velocity, while the even-numbered contribute to the stresslet.

For interfacially-driven microswimmers, a second means of controlling their motion is offered by breaking symmetries of the slip velocity. This symmetry breaking can be imposed, as when a self-phoretic particle is fabricated

with non-axisymmetric surface chemistry [53, 54], or can emerge *in situ*, due to effects of confinement [37, 55] or symmetry-breaking fields [36, 56]. So far, applications of the squirmer model have mostly been restricted to axisymmetric slip, although more general slip has been considered for spherical squirmers [57–60]. For instance, Burada *et al.* consider the far-field interaction of two spherical squirmers with a chiral distribution of slip. They find that these spheres can exhibit oscillatory “bounded states” in which they orbit around a common average trajectory [61].

THEORY

In this work, we develop a framework to study the consequences of particle shape and non-axisymmetry of the surface slip for interactions between interfacially-driven microswimmers. We develop analytical predictions in a far-field, “point-particle” model, building on the Saintillan-Shelley kinetic theory of microswimmers [62–65]. Our analytical predictions are supported by high resolution numerical calculations using the squirmer model, which resolve the finite size of the particle and near-field hydrodynamic interactions. We show that both non-spherical shape and breaking of the axisymmetry are necessary conditions to form stable “head-to-head” bound pairs. These immotile bound states are held together by (far-field) hydrodynamic interactions. Similarly, we find that motile “head-to-tail” bound pairs can be stable only when the particles are non-spherical (although they can be axisymmetric.) Overall, we find good agreement between theory and numerics, suggesting that our framework offers a promising approach for studying self-organization in heterogeneous active suspensions.

Minimal model

We model swimmer $\alpha \in \{1, 2\}$ as a point-like particle with swimming direction $\hat{d}^{(\alpha)}$ and self-propulsion velocity $U_s^{(\alpha)} \geq 0$. Swimmers are coupled by the flows they generate. The velocity of swimmer α is

$$\mathbf{U}^{(\alpha)} = U_s^{(\alpha)} \hat{d}^{(\alpha)} + \mathbf{u}(\mathbf{x}_\alpha). \quad (1)$$

In the second term, the swimmer is advected by the ambient flow, evaluated at its position \mathbf{x}_α . (The finite size of the swimmer is neglected.) For the rotation of the swimmer, we write the Jeffery equation [64]

$$\dot{\hat{d}}^{(\alpha)} = \left(\mathcal{I} - \hat{d}^{(\alpha)} \hat{d}^{(\alpha)} \right) \cdot \left(\Gamma_\alpha \mathbf{E}(\mathbf{x}_\alpha) + \mathbf{W}(\mathbf{x}_\alpha) \right) \cdot \hat{d}^{(\alpha)}. \quad (2)$$

Here, Γ_α is a shape parameter that is zero for a sphere, positive for a prolate spheroid that has its major axis aligned with $\hat{d}^{(\alpha)}$, and negative for an oblate spheroid

that has its minor axis aligned with $\hat{d}^{(\alpha)}$. The tensors $\mathbf{E}(\mathbf{x}_\alpha)$ and $\mathbf{W}(\mathbf{x}_\alpha)$ are the rate-of-strain and vorticity, respectively, evaluated at \mathbf{x}_α , where $\mathbf{E} = \frac{1}{2} (\nabla \mathbf{u} + \nabla \mathbf{u}^T)$ and $\mathbf{W} = \frac{1}{2} (\nabla \mathbf{u} - \nabla \mathbf{u}^T)$. \mathcal{I} is the identity tensor.

To model swimmer-generated flow, we associate an active “stresslet” with each swimmer. In general, the stresslet provides the slowest decaying contribution of a force-free, rigid microswimmer to the surrounding flow field. It can be obtained from the surface traction [19, 66]:

$$S_{ij}^{(\alpha)} = \frac{1}{2} \int_{\Sigma_\alpha} [\sigma_{ik} \hat{n}_k x_j + \sigma_{jk} \hat{n}_k x_i] dS - \frac{1}{3} \int_{\Sigma_\alpha} \sigma_{lk} \hat{n}_k x_l dS \delta_{ij}. \quad (3)$$

The integral is taken over the surface Σ_α of particle α , \hat{n} points from the surface of the particle into the surrounding fluid, and $\boldsymbol{\sigma} = -p\mathcal{I} + \mu(\nabla \mathbf{u} + \nabla \mathbf{u}^T)$ is the stress tensor for a Newtonian fluid. Here, $p(\mathbf{x})$ is the pressure and μ is the dynamic viscosity of the fluid. The velocity field due to a stresslet located at the origin is given by:

$$u_i = \frac{1}{8\pi\mu} \left(\frac{x_i \delta_{jk}}{r^3} - \frac{3x_i x_j x_k}{r^5} \right) S_{jk}^{(\alpha)}, \quad (4)$$

where r is distance from the origin and x_i is a location in the fluid. For a swimmer with an *axisymmetric* surface actuation, the stresslet can be written as [67]

$$\mathbf{S}^{(\alpha)} = \sigma_0^{(\alpha)} \left(\hat{d}^{(\alpha)} \hat{d}^{(\alpha)} - \frac{\mathcal{I}}{3} \right). \quad (5)$$

The sign of $\sigma_0^{(\alpha)}$ determines the “pusher” ($\sigma_0^{(\alpha)} < 0$) or “puller” ($\sigma_0^{(\alpha)} > 0$) character of the swimmer.

However, not all microswimmers have axisymmetric actuation. For instance, consider metallo-dielectric particles that are energized by an AC electric field and swim via induced charge electrophoresis (ICEP) [36]. The applied field can break axisymmetry. Thus, we consider a more general stresslet, written in a frame aligned with the principal axes \hat{c} , \hat{d} , and \hat{e} of $\mathbf{S}^{(\alpha)}$:

$$\mathbf{S}^{(\alpha)} = S_{cc}^{(\alpha)} \hat{c} \hat{c} + S_{dd}^{(\alpha)} \hat{d} \hat{d} + S_{ee}^{(\alpha)} \hat{e} \hat{e}, \quad (6)$$

with $\text{tr}(\mathbf{S}^{(\alpha)}) = 0$. Since $\mathbf{S}^{(\alpha)}$ is symmetric and real-valued, its principal axes are orthogonal, and we define $\hat{c} \times \hat{d} = \hat{e}$. This form of the stresslet tensor is generic. However, for simplicity, we make the assumption that the direction of propulsion of an isolated particle is \hat{d} , *i.e.*, aligned with a principal axis. This assumption is realized by an ICEP particle with spheroidal shape and axisymmetric metal coverage, swimming in unbounded solution (Fig. 1(a)). If the electric field is in the \hat{z} direction and the particle axis of symmetry is given by \hat{d} , the particle will rotate such that \hat{d} is perpendicular to \hat{z} [36, 40]. After rotation, the particle will swim strictly in \hat{d} with a stresslet tensor in the form of Eq. 6. A detailed technical discussion of \mathbf{S} and the assumption concerning \hat{d} is provided in the Supplemental Material (SM) [68].

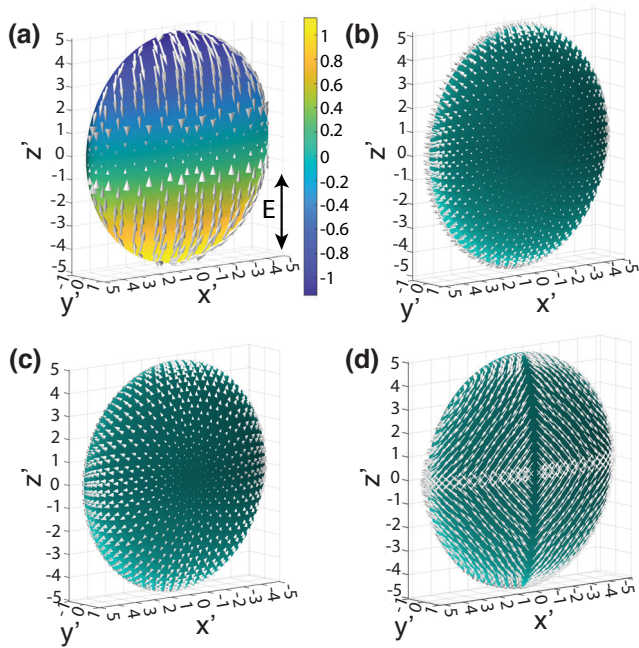


FIG. 1. (a) An oblate particle that self-propels in the presence of an AC electric field (black arrow) by ICEP. The background color indicates the electrostatic potential (arbitrary units) on the particle surface for the half-period in which the field is pointing in the negative z' direction. White arrows show the surface slip, which is non-axisymmetric. (b) Distribution of slip for the first squirmering mode B_1 . (c) Distribution of slip for B_2 . (d) Non-axisymmetric slip for \tilde{B} , following the definition in Eq. 7. In all panels, $r_e = 5$.

Additionally, we note that Eq. 6 reduces to Eq. 5 when $S_{dd}^{(\alpha)} = 2/3\sigma_0$ and $S_{cc}^{(\alpha)} = S_{ee}^{(\alpha)} = -\sigma_0/3$.

In the following, we restrict our consideration to two swimmers moving in the xy plane, and study conditions for obtaining stable bound states. The instantaneous configuration of the system is specified by the center-to-center distance d and the angles ϕ_1 and ϕ_2 , where ϕ_α is the angle between $\hat{d}^{(\alpha)}$ and a fixed axis, chosen as the x -axis (see Fig. 1 in the SM). We assume that $\hat{c}^{(\alpha)}$ and $\hat{d}^{(\alpha)}$ lie within the xy plane. For convenience, we specify that swimmer 1 is instantaneously at $\mathbf{x}_1 = (0, 0, 0)$. Swimmer 2 has position $\mathbf{x}_2 = (x, y, 0)$. We construct \hat{x} , \hat{y} , $\hat{\phi}_1$, and $\hat{\phi}_2$ as functions of x , y , ϕ_1 , and ϕ_2 , and look for fixed point configurations at which these functions evaluate to zero, representing a bound state. For simplicity, we consider only bound states in which the propulsion axes are aligned with the center-to-center axis.

The point-particle model is analytically tractable and yields a wealth of predictions. However, we wish to compare these predictions against numerical results that account for finite size and do not truncate the particle-generated flow field to the leading-order term.

Squirmer model

We consider $N \in \{1, 2\}$ spheroidal particles in unbounded Newtonian fluid. Following Ref. 52, for particle α , we take the length of the semi-axis of symmetry to define $b_y^{(\alpha)}$, and the length of the other semi-axes to define $b_x^{(\alpha)}$. Thus, each particle has an aspect ratio $r_e^{(\alpha)}$ defined by $r_e \equiv b_x/b_y$, with $r_e < 1$ for an prolate spheroid, $r_e = 1$ for a sphere, and $r_e > 1$ for an oblate spheroid. The quantity Γ_α is related to $r_e^{(\alpha)}$ by $\Gamma = (1-r_e^2)/(1+r_e^2)$. The characteristic size of the particle, $L_0^{(\alpha)}$, is chosen as $b_y^{(\alpha)}$.

The center of particle α is located at \mathbf{x}_α . The fluid velocity $\mathbf{u}(\mathbf{x})$ is governed by the Stokes equation $-\nabla p + \mu\nabla^2\mathbf{u} = 0$ and the incompressibility condition $\nabla \cdot \mathbf{u} = 0$. On the surface Σ_α of particle α , the velocity obeys $\mathbf{u} = \mathbf{U}^{(\alpha)} + \boldsymbol{\Omega}^{(\alpha)} \times (\mathbf{x} - \mathbf{x}_\alpha) + \mathbf{v}_s^{(\alpha)}(\mathbf{x})$. Additionally, $|\mathbf{u}| \rightarrow 0$ as $|\mathbf{x}| \rightarrow \infty$. Each particle is force-free and torque-free: $\int_{\Sigma_\alpha} \boldsymbol{\sigma} \cdot \hat{\mathbf{n}} dS = 0$ and $\int_{\Sigma_\alpha} (\mathbf{x} - \mathbf{x}_\alpha) \times \boldsymbol{\sigma} \cdot \hat{\mathbf{n}} dS = 0$.

For each swimmer, the slip $\mathbf{v}_s^{(\alpha)}$ is fixed in a frame attached to the swimmer. It is specified via a set of squirmering mode amplitudes. In previous work, we generalized the axisymmetric squirmering modes to spheroidal particles. The amplitudes are denoted by $B_i^{(\alpha)}$, with $i \geq 1$ [52], and here are assumed to be given in units of an arbitrary characteristic velocity. The first two modes are shown in Fig. 1(b) and (c). Here, in order to break axisymmetry, we develop a new squirmering mode $\tilde{B}^{(\alpha)}$ inspired by the slip profile of ICEP particles. This squirmering mode has slip distribution

$$\mathbf{v}_s^{(\alpha)}(\mathbf{x}) = \tilde{B}^{(\alpha)}[\text{sign}(z')(\cos(\varphi)\hat{e}_\xi - \hat{e}_\varphi(\hat{e}_\xi \cdot \hat{e}_{z'})) - \text{sign}(x')(\sin(\varphi)\hat{e}_\xi - \hat{e}_\varphi(\hat{e}_\xi \cdot \hat{e}_{x'}))] \cdot H(y'), \quad (7)$$

shown in Fig. 1(d). Here, $H(y')$ is the step function, and \hat{e}_φ and \hat{e}_ξ are two surface tangential basis vectors in a particle-centered spheroidal coordinate system. (The prime symbol is used to distinguish the coordinate system in Fig. 1 from the coordinate system used for studying pair interactions.)

We briefly discuss the properties of a single squirmer. From solution of the governing equations, we obtain U_s and \mathbf{S} for a given r_e and set of squirmering mode amplitudes. Due to the linearity of the Stokes equation, the contribution of each squirmering mode can be calculated individually and superposed. For the axisymmetric modes, Fig. 2 in the SM shows how the B_i contribute to $U_s^{(\alpha)}$ and $\sigma_0^{(\alpha)}$. For the non-axisymmetric mode, we show $S_{cc}^{(\alpha)}$, $S_{dd}^{(\alpha)}$ and $S_{ee}^{(\alpha)}$ as a function of r_e in SM Fig. 5. This squirmering mode makes no contribution to $S_{dd}^{(\alpha)}$ or $U_s^{(\alpha)}$, and contributes anti-symmetrically to $S_{cc}^{(\alpha)}$ and $S_{ee}^{(\alpha)}$.

For $N = 2$, we solve for the particle velocities numerically, using the boundary element method (BEM) [69].

We obtain trajectories using a rigid body dynamics engine [42]. For simplicity, we assume that $L_0^{(1)} = L_0^{(2)}$. (The point-particle model has no inherent length scale. Since $S_{ij} \sim L_0^3$ and $U_s \sim L_0^2$ for a squirmer, differences in size can be straightforwardly accommodated in our model.)

RESULTS

Head-to-head pairing

We look for fixed point solutions of the point-particle model with $(x, y, \phi_1, \phi_2) = (d_0, 0, 0, \pi)$. Through a detailed derivation in the SM, we obtain

$$d_0 = \sqrt{\frac{-3(S_{dd}^{(1)} + S_{dd}^{(2)})}{8\pi\mu(U_s^{(1)} + U_s^{(2)})}}. \quad (8)$$

Given that $U_s^{(\alpha)} > 0$, to obtain a finite separation $d > 0$, it is required that $(S_{dd}^{(1)} + S_{dd}^{(2)}) < 0$. In other words, the pair must have a net ‘‘pusher’’ character. In the SM, we present a general linear stability analysis. Here, we discuss identical swimmers, i.e., $U_s^{(1)} = U_s^{(2)}$, $\mathbf{S}^{(1)} = \mathbf{S}^{(2)}$, and $\Gamma_1 = \Gamma_2$. As conditions for stability, we obtain $\Gamma < -1/3$ and $[S_{cc}(-1+\Gamma) + S_{dd}(1+2\Gamma)][S_{cc}(-1+\Gamma) - S_{dd}(1+4\Gamma)] < 0$, given that $S_{dd} < 0$. Notably, the requirement $\Gamma < -1/3$ corresponds to an oblate shape, recalling the discoidal particles in Ref. 35. Intriguingly, head-to-head pairing cannot be obtained for *axisymmetric* swimmers (Eq. 5). For $S_{dd} = 2\sigma_0/3$ and $S_{cc} = S_{ee} = -\sigma_0/3$, with $\sigma_0 < 0$, the second condition reduces to $\Gamma > -1/9$. This cannot be reconciled with $\Gamma < -1/3$. Thus, this work completes the analysis of Ref. 35, which assumed an axisymmetric stresslet. Here, we have shown that non-axisymmetry is a necessary ingredient in the pairing observed in Ref. 35.

To further investigate deviation from axisymmetry, we consider stresslets of the form

$$\mathbf{S} = \mathbf{S}_{ax} + \sigma_0 \delta (\hat{c}\hat{c} - \hat{e}\hat{e}), \quad (9)$$

where \mathbf{S}_{ax} is equal to the right hand side of Eq. 5, and δ is dimensionless. We obtain $\Gamma < -1/3$ and $(-1 + 3\Gamma(-3 + \delta) - 3\delta)(1 + \Gamma + \delta(-1 + \Gamma)) < 0$. Notably, these requirements are independent of σ_0 and U_s . In Fig. 2(a), the background color shows the predicted phase map. We also show two types of numerical data. Crosses represent squirmers with a non-axisymmetric squirmering mode. This mode introduces the perturbation δ in a controllable manner (see Fig. 5 in the SM). Circles show the results for an effective squirmer model for ICEP particles. Red symbols indicate pairs without a stable bound state. The theoretical and numerical results largely agree with each other. The one area of significant mismatch is

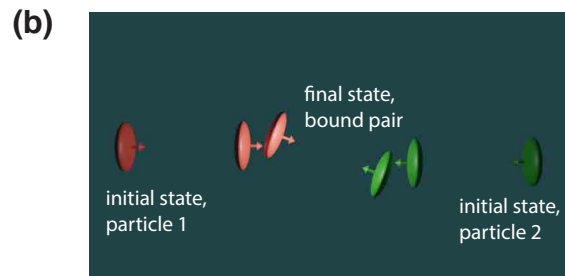
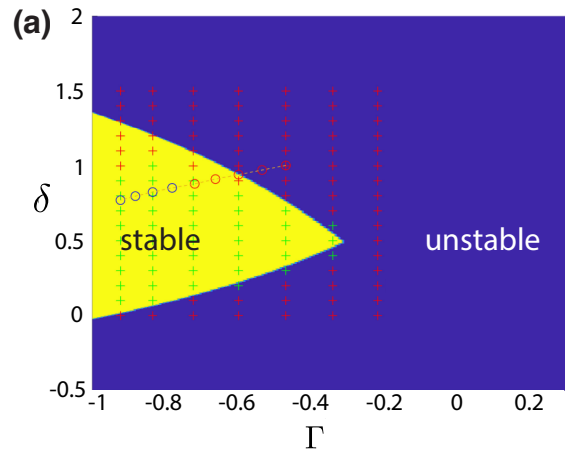


FIG. 2. (a) Phase map for head-to-head pairs. The background colors show the stability predicted by the analytical model. Crosses represent the results of numerical calculations for non-axisymmetric squirmers (Eq. 7) with modes $B_1^{(\alpha)} = 0.1$, $B_2^{(\alpha)} = -1$ and varying \tilde{B} and Γ . Circles indicate numerical data for the ICEP effective squirmer model, and are connected by a line to guide the eye. Green and blue symbols indicate pairs with a stable bound state; red symbols represent unstable pairs. (b) Trajectory obtained for $\Gamma = -0.835$ and $\tilde{B} = 1.68$.

for $\Gamma \approx -1$, i.e., oblate spheroids with large r_e . Recalling that b_y was chosen as a characteristic length, oblate particles with large r_e also have large b_x . When $b_x \gg d_0$, the point particle assumption is expected to be erroneous. In Fig. 2(b), we show pair formation for $\Gamma = -0.835$ and $\tilde{B} = 1.68$.

The condition $\Gamma < -1/3$ has a straightforward physical interpretation. At the location of a particle, the rate-of-strain tensor \mathbf{E} has two principal axes. Spheroidal particles tend to align their long axes with the local axis of extension [70, 71]. For an axisymmetric stresslet (Eq. 5) located at the origin and oriented in the x-direction, we evaluate \mathbf{E}_{ax} at the position $x = d$, $y = 0$. From the eigenvalues and eigenvectors of this quantity, we find that the axis of extension is indeed in the y-direction. Thus, the straining component of flow will tend to stabilize the orientation of oblate spheroids in a head-on collision. Furthermore, we note that δ does not appear in the condition $\Gamma < -1/3$. As a consistency check, we form the

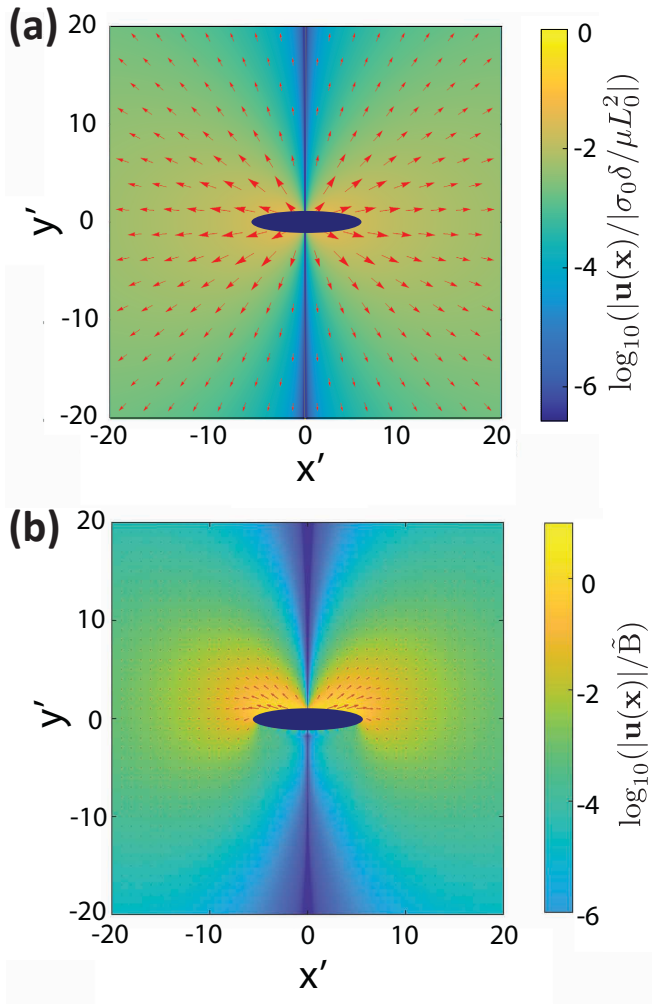


FIG. 3. (a) Flow field due to a non-axisymmetric stresslet located at the origin, with \hat{c} in the x' direction and \hat{e} in the z' direction. The direction of the flow is shown for the case $\sigma_0\delta < 0$. The flow is radially outward, but the magnitude is anisotropic. An oblate spheroid is shown for comparison with (b). (b) Flow field due to the non-axisymmetric \hat{B} mode for the oblate spheroidal particle shown in Fig. 1(d). In both (a) and (b), the flow velocity is zero at $x' = 0$.

rate-of-strain tensor \mathbf{E}_δ for the non-axisymmetric contribution to flow (second term in Eq. 9), assuming that $\hat{d} = \hat{x}$ and $\hat{c} = -\hat{y}$. We find that it indeed evaluates to zero at $x = d$, $y = 0$. Additionally, in Fig. 3(a), we plot the flow from the idealized non-axisymmetric stresslet. On the \hat{d} axis (in the figure, the y' axis), it evaluates to zero, which explains why d_0 is determined by the axisymmetric component of the stresslet (Eq. 8).

The second requirement for linear stability, $(-1 + 3\Gamma(-3 + \delta) - 3\delta)(1 + \Gamma + \delta(-1 + \Gamma)) < 0$, is more difficult to interpret. The quantities Γ and δ are implicated, both individually and as a product with each other. Additionally, by introducing dummy variables into the Jacobian, we have confirmed that both vorticity and transverse ad-

vection (*i.e.*, motion in y , transverse to the center-to-center vector) contribute to this condition. Some insight can be obtained from the form of the Jacobian in SM Eq. 40. The stresslet component S_{cc} appears only in off-diagonal terms that couple transversal displacements and particle rotations. This suggests that the non-axisymmetric stresslet is important in the intricate dance in which particles simultaneously rotate to face each other and slide laterally into register, as shown in Fig. 2 (b). In contrast, it is known that spherical squirmers in a head-on collision are unstable to maneuvering past each other in a process involving rotations and transversal motion [35]. Looking at the flow for the non-axisymmetric stresslet in Fig. 3(a), some stabilizing roles of this radially outward flow may be in hindering the particles from moving past each other and in contributing to alignment. Regarding alignment, we recall that the magnitude and sign of the contribution of the rate-of-strain tensor to rotation is controlled by the shape parameter Γ (Eq. 2). We also note that while the flow fields close to the particle can differ significantly between the idealized non-axisymmetric stresslet in Fig. 3(a) and the non-axisymmetric squirming mode in Fig. 3(b), far from the particle, both flow fields are radially outward.

Head-to-tail pairs

Now we look for fixed point solutions with $(x, y, \phi_1, \phi_2) = (d_0, 0, 0, 0)$. We obtain

$$d_0 = \sqrt{\frac{3(S_{dd}^{(1)} + S_{dd}^{(2)})}{8\pi\mu(U_s^{(2)} - U_s^{(1)})}}. \quad (10)$$

Notably, the two particles must have unequal speeds U_s for $d_0 > 0$. The bound pair moves with a steady speed given by Eq. 27 in the SM. Regarding stability against displacements in x , we again obtain the “net pusher” condition $(S_{dd}^{(1)} + S_{dd}^{(2)}) < 0$. From Eq. 10, this implies $U_s^{(1)} > U_s^{(2)}$. The other stability conditions are $S_{dd}^{(2)}(1 + 3\Gamma_1) + S_{dd}^{(1)}(1 + \Gamma_2) > 0$ and Eq. 48 in the SM. For axisymmetric swimmers, we can obtain stable pairing. Specifically, $\sigma_0^{(1)} + \sigma_0^{(2)} + 3(\sigma_0^{(2)}\Gamma_1 + \sigma_0^{(1)}\Gamma_2) > 0$ and Eq. 13 in the SI. Overall, the phase behavior is determined by four parameters: Γ_1 , Γ_2 , $S \equiv \sigma_0^{(2)}/\sigma_0^{(1)}$, and $V \equiv U_s^{(2)}/U_s^{(1)}$. For the slice of phase space in Fig. 4 (a), we fix $V = 0.8$ and $\Gamma_2 = -0.8$, but vary Γ_1 and S . In the numerics, B_1 and B_2 are chosen to vary S while keeping $V = 0.8$. The model has good agreement with the numerics. There are two areas of significant disagreement. Similar to head-to-head pairs, one is for oblate particles with large r_e . The other is the slim area bordering $S = -1$, where $d_0 \rightarrow 0$. An example trajectory is shown in Fig. 4 (b).

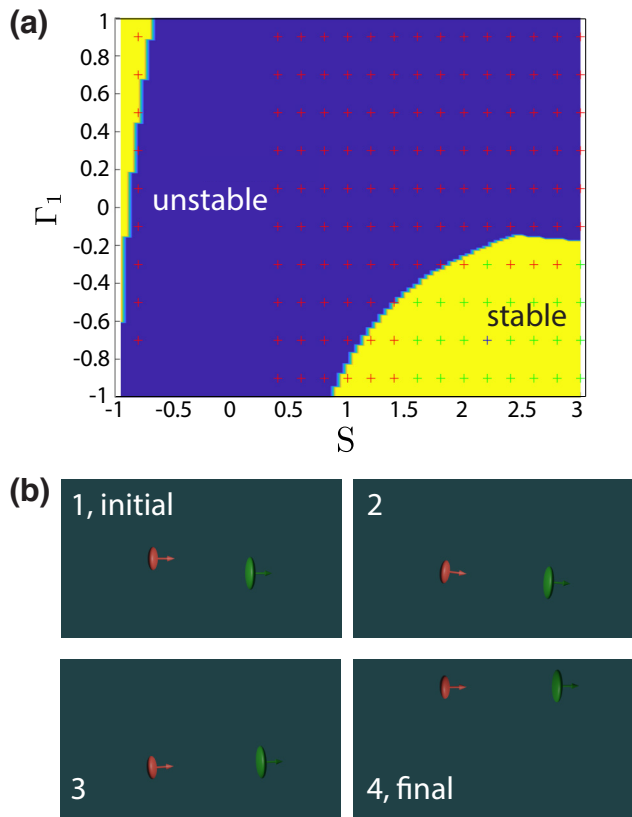


FIG. 4. (a) Phase map for head-to-tail pairs with $\Gamma_2 = -0.8$ and $V = 0.8$ and varying S and Γ_1 . The background colors show the stability predicted by our model and symbols represent the results of numerical calculations. Green and blue symbols indicate pairs with a stable bound state; red symbols indicate pairs without a stable bound state. (b) Snapshots of an example trajectory for $S = 2.2$ and $\Gamma_1 = -0.7$. This pair is represented by a blue cross in (a). The particles are initially separated by $x_{2,\text{initial}} = 3$ and $y_{2,\text{initial}} = 20$.

CONCLUSIONS

We have shown that non-spherical active particles can form bound pairs through far-field hydrodynamic interactions. A surprising finding of our work is that squirmlers with non-axisymmetric surface slip may be capable of pairing behaviors that are *not* obtainable for squirmlers with axisymmetric slip.

We restricted our consideration to swimmers moving in the plane containing their center-to-center vector (the xy plane). For non-axisymmetric particles defined by Eq. 9, a 90° rotation of both particles around their \hat{d} axes will invert the sign of δ . Therefore, when head-to-head bound states, aligned with x , are stable against perturbations in the xy plane, they will be unstable in the yz plane. However, our quasi-2D assumption is realized in most active matter experiments. For head-to-tail pairs of axisymmetric particles, the stability conditions found here apply to general three-dimensional motions.

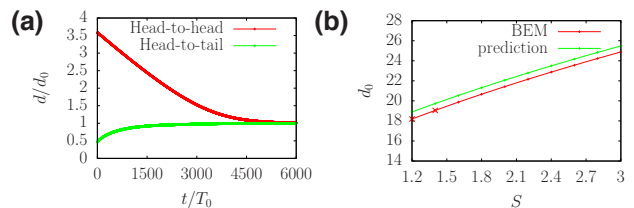


FIG. 5. (a) Separation d for two squirmlers forming a stable bound state. For the head-to-tail pair, $\Gamma_1 = -0.7$, $\Gamma_2 = -0.8$, $S = 2.2$ and $U = 0.8$, with $x_{2,\text{initial}} = 3$ and $y_{2,\text{initial}} = 10$. For the head-to-head pair, $B_1 = 0.1$, $B_2 = -1$, $\tilde{B} = 1.6833$ and $\Gamma = -0.835$, with $x_{\text{initial}} = 2$ and $y_{\text{initial}} = 55$. The particle parameters correspond to Figs. 2 (b) and 4 (b), respectively. (b) The predicted and numerically calculated steady separations for head-to-tail pairs with $\Gamma_1 = -0.7$, $\Gamma_2 = -0.8$, $V = 0.8$ and varying S , corresponding to the second row from the bottom in Fig. 4 (a). Symbols indicate values of S for which theory and numerics disagree concerning stability.

Future work could incorporate the effects of inertia and/or near-field hydrodynamic interactions [25, 72]. Lubrication interactions can induce bound states for spherical squirmlers near contact [21, 25]. Additionally, making use of the Faxén relations for spheroids would account for the finite size of a particle in its response to ambient flow [66, 73]. Our model may have stable bound states in which particle orientations are not aligned in the direction of propulsion. Finally, the bound states found here may have implications for hierarchical self-organization and collective behavior. For instance, Ref. 35 observed that initial formation of immotile head-to-head bound states locally promoted formation of additional bound states in a feedback loop, ultimately leading to phase separation. This mechanism could be studied in the framework of the present work.

ACKNOWLEDGMENTS

We gratefully acknowledge donors of the American Chemical Society Petroleum Research Fund for support of this research through Grant No. 60809-DNI9. This research was also sponsored by the Army Research Office and was accomplished under Grant Number W911NF-23-1-0190. The views and conclusions contained in this document are those of the authors and should not be interpreted as representing the official policies, either expressed or implied, of the Army Research Office or the U.S. Government. The U.S. Government is authorized to reproduce and distribute reprints for Government purposes notwithstanding any copyright notation herein. The technical support and advanced computing resources from University of Hawaii Information Technology Services – Cyberinfrastructure, funded in part by the National Science Foundation CC* awards #2201428 and

#2232862 are gratefully acknowledged. We also thank Rumen Georgiev for insightful discussions.

* uspal@hawaii.edu

- [1] T. Sanchez, D. T. Chen, S. J. DeCamp, M. Heymann, and Z. Dogic, Spontaneous motion in hierarchically assembled active matter, *Nature* **491**, 431 (2012).
- [2] A. Aubret, M. Youssef, S. Sacanna, and J. Palacci, Targeted assembly and synchronization of self-spinning microgears, *Nature Physics* **14**, 1114 (2018).
- [3] A. M. Boymelgreen, T. Balli, T. Miloh, and G. Yossifon, Active colloids as mobile microelectrodes for unified label-free selective cargo transport, *Nature communications* **9**, 760 (2018).
- [4] P. Arora, A. K. Sood, and R. Ganapathy, Emergent stereoselective interactions and self-recognition in polar chiral active ellipsoids, *Science Advances* **7**, eabd0331 (2021).
- [5] J. Palacci, S. Sacanna, A. P. Steinberg, D. J. Pine, and P. M. Chaikin, Living crystals of light-activated colloidal surfers, *Science* **339**, 936 (2013).
- [6] I. Buttinoni, J. Bialké, F. Kümmel, H. Löwen, C. Bechinger, and T. Speck, Dynamical clustering and phase separation in suspensions of self-propelled colloidal particles, *Phys. Rev. Lett.* **110**, 238301 (2013).
- [7] O. Pohl and H. Stark, Dynamic clustering and chemotactic collapse of self-phoretic active particles, *Phys. Rev. Lett.* **112**, 238303 (2014).
- [8] M. E. Cates and J. Tailleur, Motility-induced phase separation, *Annu. Rev. Condens. Matter Phys.* **6**, 219 (2015).
- [9] B. V. Hokmabad, A. Nishide, P. Ramesh, C. Krüger, and C. C. Maass, Spontaneously rotating clusters of active droplets, *Soft Matter* **18**, 2731 (2022).
- [10] A. Bricard, J. Caussin, N. Desreumaux, O. Dauchot, and D. Bartolo, Emergence of macroscopic directed motion in populations of motile colloids, *Nature* **503**, 95 (2013).
- [11] J. Yan, M. Han, J. Zhang, C. Xu, E. Luijten, and S. Granick, Reconfiguring active particles by electrostatic imbalance, *Nature materials* **15**, 1095 (2016).
- [12] A. Kaiser, A. Snezhko, and I. S. Aranson, Flocking ferromagnetic colloids, *Science Advances* **3**, e1601469 (2017).
- [13] K. Han, G. Kokot, O. Tovkach, A. Glatz, I. S. Aranson, and A. Snezhko, Emergence of self-organized multivortex states in flocks of active rollers, *Proceedings of the National Academy of Sciences* **117**, 9706 (2020).
- [14] J. Zhang, R. Alert, J. Yan, N. Wingreen, and S. Granick, Active phase separation by turning towards regions of higher density, *Nat. Phys.* **17** (2021).
- [15] F. Martínez-Pedrero and P. Tierno, Advances in colloidal manipulation and transport via hydrodynamic interactions, *Journal of Colloid and Interface Science* **519**, 296 (2018).
- [16] M. J. Lighthill, On the squirming motion of nearly spherical deformable bodies through liquids at very small reynolds numbers, *Commun. Pure Appl. Math.* **5**, 109 (1952).
- [17] J. R. Blake, A spherical envelope approach to ciliary propulsion, *J. Fluid Mech.* **46**, 199 (1971).
- [18] T. J. Pedley, Spherical squirmers: models for swimming micro-organisms, *IMA Journal of Applied Mathematics* **81**, 488 (2016).
- [19] T. Ishikawa, M. Simmonds, and T. J. Pedley, Hydrodynamic interaction of two swimming model micro-organisms, *Journal of Fluid Mechanics* **568**, 119 (2006).
- [20] T. Ishikawa and T. Pedley, Diffusion of swimming model micro-organisms in a semi-dilute suspension, *Journal of Fluid Mechanics* **588**, 437 (2007).
- [21] K. Drescher, K. C. Leptos, I. Tuval, T. Ishikawa, T. J. Pedley, and R. E. Goldstein, Dancing Volvox: Hydrodynamic bound states of swimming algae, *Phys. Rev. Lett.* **102**, 168101 (2009).
- [22] I. Llopis and I. Pagonabarraga, Hydrodynamic interactions in squirmer motion: Swimming with a neighbour and close to a wall, *Journal of Non-Newtonian Fluid Mechanics* **165**, 946 (2010).
- [23] K. Ishimoto and E. A. Gaffney, Squirmer dynamics near a boundary, *Physical Review E* **88**, 062702 (2013).
- [24] G.-J. Li and A. M. Ardekani, Hydrodynamic interaction of microswimmers near a wall, *Physical Review E* **90**, 013010 (2014).
- [25] C. Darveniza, T. Ishikawa, T. J. Pedley, and D. R. Brumley, Pairwise scattering and bound states of spherical microorganisms, *Phys. Rev. Fluids* **7**, 013104 (2022).
- [26] V. Magar, T. Goto, and T. J. Pedley, Nutrient uptake by a self-propelled steady squirmer, *The Quarterly Journal of Mechanics and Applied Mathematics* **56**, 65 (2003).
- [27] S. Michelin and E. Lauga, Optimal feeding is optimal swimming for all péclet numbers, *Physics of Fluids* **23**, 101901 (2011).
- [28] Y. Wang, R. M. Hernandez, D. J. Bartlett, J. M. Bingham, T. R. Kline, A. Sen, and T. E. Mallouk, Bipolar electrochemical mechanism for the propulsion of catalytic nanomotors in hydrogen peroxide solutions, *Langmuir* **22**, 10451 (2006).
- [29] J. R. Howse, R. A. Jones, A. J. Ryan, T. Gough, R. Vafabakhsh, and R. Golestanian, Self-motile colloidal particles: from directed propulsion to random walk, *Physical review letters* **99**, 048102 (2007).
- [30] H.-R. Jiang, N. Yoshinaga, and M. Sano, Active motion of a Janus particle by self-thermophoresis in a defocused laser beam, *Physical review letters* **105**, 268302 (2010).
- [31] A. P. Bregulla and F. Cichos, Flow fields around pinned self-thermophoretic microswimmers under confinement, *The Journal of chemical physics* **151**, 044706 (2019).
- [32] M. Popescu, W. Uspal, Z. Eskandari, M. Tasinkevych, and S. Dietrich, Effective squirmer models for self-phoretic chemically active spherical colloids, *Eur. Phys. J. E* **41**, 145 (2018).
- [33] E. Lauga and S. Michelin, Stresslets induced by active swimmers, *Phys. Rev. Lett.* **117**, 148001 (2016).
- [34] H. A. Stone and A. D. T. Samuel, Propulsion of microorganisms by surface distortions, *Phys. Rev. Lett.* **77**, 4102 (1996).
- [35] J. Katuri, R. Poehnl, A. Sokolov, W. Uspal, and A. Snezhko, Arrested-motility states in populations of shape-anisotropic active Janus particles, *Science Advances* **8**, eabo3604 (2022).
- [36] T. M. Squires and M. Z. Bazant, Breaking symmetries in induced-charge electro-osmosis and electrophoresis, *J. Fluid Mech.* **560**, 65 (2006).
- [37] M. S. Kilic and M. Z. Bazant, Induced-charge electrophoresis near a wall, *Electrophoresis* **32**, 614–628 (2011).
- [38] A. M. Brooks, S. Sabrina, and K. J. Bishop, Shape-directed dynamics of active colloids powered by induced-

- charge electrophoresis, Proceedings of the national academy of sciences **115**, E1090 (2018).
- [39] P. Sharan, C. Maslen, B. Altunkeyik, I. Rehor, J. Simmchen, and T. D. Montenegro-Johnson, Fundamental modes of swimming correspond to fundamental modes of shape: Engineering i-, u-, and s-shaped swimmers, *Advanced Intelligent Systems* **3**, 2100068 (2021).
- [40] N. M. Diwakar, G. Kunti, T. Miloh, G. Yossifon, and O. D. Velev, Ac electrohydrodynamic propulsion and rotation of active particles of engineered shape and asymmetry, *Current Opinion in Colloid & Interface Science*, 101586 (2022).
- [41] A. Ganguly and A. Gupta, Going in circles: Slender body analysis of a self-propelling bent rod, *Physical Review Fluids* **8**, 014103 (2023).
- [42] M. Theers, E. Westphal, G. Gompper, and R. G. Winkler, Modeling a spheroidal microswimmer and cooperative swimming in a narrow slit, *Soft Matter* **12**, 7372 (2016).
- [43] S. Michelin and E. Lauga, Geometric tuning of self-propulsion for Janus catalytic particles, *Scientific reports* **7**, 1 (2017).
- [44] E. Yariv, Self-diffusiophoresis of slender catalytic colloids, *Langmuir* **36**, 6903 (2019).
- [45] A. Daddi-Moussa-Ider, B. Nasouri, A. Vilfan, and R. Golestanian, Optimal swimmers can be pullers, pushers or neutral depending on the shape, *Journal of Fluid Mechanics* **922**, R5 (2021).
- [46] R. Poehnl and W. Uspal, Phoretic self-propulsion of helical active particles, *Journal of Fluid Mechanics* **927**, A46 (2021).
- [47] A. W. Zantop and H. Stark, Emergent collective dynamics of pusher and puller squirmer rods: swarming, clustering, and turbulence, *Soft Matter* **18**, 6179 (2022).
- [48] M. Bär, R. Großmann, S. Heidenreich, and F. Peruani, Self-propelled rods: Insights and perspectives for active matter, *Annual Review of Condensed Matter Physics* **11**, 441 (2020).
- [49] B. Felderhof, Stokesian swimming of a prolate spheroid at low Reynolds number, *European Journal of Mechanics-B/Fluids* **60**, 230 (2016).
- [50] A. M. Leshansky, O. Kenneth, O. Gat, and J. E. Avron, A frictionless microswimmer, *New Journal of Physics* **9**, 145 (2007).
- [51] T. Ishikawa and M. Hota, Interaction of two swimming paramecia, *Journal of Experimental Biology* **209**, 4452 (2006).
- [52] R. Pöhl, M. N. Popescu, and W. E. Uspal, Axisymmetric spheroidal squirmers and self-diffusiophoretic particles, *J. Phys.: Condens. Matter* **32**, 164001 (2020).
- [53] R. Archer, A. Campbell, and S. Ebbens, Glancing angle metal evaporation synthesis of catalytic swimming Janus colloids with well defined angular velocity, *Soft Matter* **11**, 6872 (2015).
- [54] M. Lisicki, S. Y. Reigh, and E. Lauga, Autophoretic motion in three dimensions, *Soft Matter* **14**, 3304 (2018).
- [55] W. E. Uspal, M. N. Popescu, S. Dietrich, and M. Tasinkevych, Self-propulsion of a catalytically active particle near a planar wall: from reflection to sliding and hovering, *Soft Matter* **11**, 434 (2015).
- [56] M. N. Popescu, W. E. Uspal, C. Bechinger, and P. Fischer, Chemotaxis of active Janus nanoparticles, *Nano letters* **18**, 5345 (2018).
- [57] S. Ghose and R. Adhikari, Irreducible representations of oscillatory and swirling flows in active soft matter, *Phys. Rev. Lett.* **112**, 118102 (2014).
- [58] O. Pak and E. Lauga, Generalized squirming motion of a sphere, *J. Eng. Math.* **88**, 1 (2014).
- [59] B. Felderhof and R. Jones, Stokesian swimming of a sphere at low Reynolds number by helical surface distortion, *Physics of Fluids* **28**, 073601 (2016).
- [60] T. J. Pedley, D. R. Brumley, and R. E. Goldstein, Squirmers with swirl: a model for volvox swimming, *Journal of Fluid Mechanics* **798**, 165–186 (2016).
- [61] P. Burada, R. Maity, and F. Jülicher, Hydrodynamics of chiral squirmers, *Physical Review E* **105**, 024603 (2022).
- [62] D. Saintillan and M. J. Shelley, Orientational order and instabilities in suspensions of self-locomoting rods, *Physical review letters* **99**, 058102 (2007).
- [63] D. Saintillan and M. J. Shelley, Instabilities, pattern formation, and mixing in active suspensions, *Physics of Fluids* **20** (2008).
- [64] D. Saintillan and M. Shelley, Active suspensions and their nonlinear models, *Comptes Rendus Physique* **14**, 497 (2013).
- [65] E. Lushi and C. S. Peskin, Modeling and simulation of active suspensions containing large numbers of interacting micro-swimmers, *Computers & Structures* **122**, 239 (2013).
- [66] S. Kim and S. J. Karrila, *Microhydrodynamics: principles and selected applications* (Courier Corporation, 2013).
- [67] D. Saintillan, Rheology of active fluids, *Ann. Rev. Fluid Mech.* **50**, 563–92 (2017).
- [68] See Supplemental Material at <http://link.aps.org/supplemental/XXX> for technical discussion of the stresslet tensor, detailed mathematical derivations of results given in the main text, details concerning implementation of the spheroidal squirmer model, and numerical results obtained with the spheroidal squirmer model. The Supplemental Material also contains Refs. 35, 37, 52, 74.
- [69] C. Pozrikidis, *A Practical Guide to Boundary Element Methods with the Software Library BEMLIB* (CRC Press, Boca Raton, 2002).
- [70] G. B. Jeffery, The motion of ellipsoidal particles immersed in a viscous fluid, *Proceedings of the Royal Society of London. Series A, Containing papers of a mathematical and physical character* **102**, 161 (1922).
- [71] M. D. Graham, *Microhydrodynamics, Brownian motion, and complex fluids*, Vol. 58 (Cambridge University Press, 2018).
- [72] Z. Ouyang, Z. Lin, J. Lin, Z. Yu, and N. Phan-Thien, Cargo carrying with an inertial squirmer in a newtonian fluid, *Journal of Fluid Mechanics* **959**, A25 (2023).
- [73] I. L. Claeyss and J. F. Brady, Suspensions of prolate spheroids in stokes flow. part 1. dynamics of a finite number of particles in an unbounded fluid, *Journal of Fluid Mechanics* **251**, 411 (1993).
- [74] G. Dassios, M. Hadjinicolaou, and A. Payatakes, Generalized eigenfunctions and complete semiseparable solutions for stokes flow in spheroidal coordinates, *Quarterly of Applied Mathematics* **52**, 157 (1994).

Supplementary Material: Shape-induced pairing of spheroidal squirmers

Ruben Poehnl¹ and William E. Uspal^{1,*}

*¹Department of Mechanical Engineering,
University of Hawai'i at Mānoa, 2540 Dole Street,
Holmes Hall 302, Honolulu, Hawaii 96822, USA*

(Dated: October 31, 2023)

arXiv:2306.01168v2 [cond-mat.soft] 30 Oct 2023

MINIMAL MODEL: COLLINEAR BOUND STATES

For a pair of spheroids, the three degrees of freedom ϕ_1 , ϕ_2 , and $d = |\mathbf{x}|$ are schematically illustrated in Fig. 1. We choose to measure ϕ_1 and ϕ_2 with respect to the x-axis in the

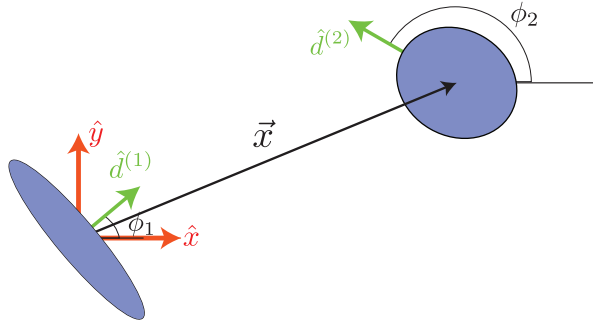


FIG. 1. Schematic illustration of the three degrees of freedom ϕ_1 , ϕ_2 , and $d = |\mathbf{x}|$ for a pair of spheroids.

laboratory frame. Without loss of generality, we choose to place the origin at the instantaneous position of particle 1. Therefore, the position of particle 1 is $\mathbf{x}_1 = (0, 0, 0)$, and the position of particle 2 is $\mathbf{x}_2 = (x, y, 0)$. In the following, the vector $\mathbf{x} \equiv \mathbf{x}_2 - \mathbf{x}_1$, and $d = |\mathbf{x}| = \sqrt{x^2 + y^2}$.

Although there are three degrees of freedom, for analytical convenience, we choose to consider the time evolution of four variables: x , y , ϕ_1 , and ϕ_2 . First, using $\text{tr}(\mathbf{S}) = 0$ and Eq. 1 in the main text, we note that

$$\dot{x}_1 = U_s^{(1)} \cos(\phi_1) + \frac{3x \left(x_i S_{ij}^{(2)} x_j \right)}{8\pi\mu d^5} \quad (1)$$

$$\dot{y}_1 = U_s^{(1)} \sin(\phi_1) + \frac{3y \left(x_i S_{ij}^{(2)} x_j \right)}{8\pi\mu d^5} \quad (2)$$

$$\dot{x}_2 = U_s^{(2)} \cos(\phi_2) - \frac{3x \left(x_i S_{ij}^{(1)} x_j \right)}{8\pi\mu d^5} \quad (3)$$

$$\dot{y}_2 = U_s^{(2)} \sin(\phi_2) - \frac{3y \left(x_i S_{ij}^{(1)} x_j \right)}{8\pi\mu d^5}, \quad (4)$$

where the Einstein summation convention is assumed for repeated subscripts. Given that $\dot{x} = \dot{x}_2 - \dot{x}_1$ and $\dot{y} = \dot{y}_2 - \dot{y}_1$, it follows that the governing equations for the four variables

x , y , ϕ_1 , and ϕ_2 are as follows:

$$\dot{x} = U_s^{(2)} \cos(\phi_2) - U_s^{(1)} \cos(\phi_1) - \frac{3x \left(x_i S_{ij}^{(1)} x_j + x_i S_{ij}^{(2)} x_j \right)}{8\pi\mu(x^2 + y^2)^{5/2}}, \quad (5)$$

$$\dot{y} = U_s^{(2)} \sin(\phi_2) - U_s^{(1)} \sin(\phi_1) - \frac{3y \left(x_i S_{ij}^{(1)} x_j + x_i S_{ij}^{(2)} x_j \right)}{8\pi\mu(x^2 + y^2)^{5/2}}, \quad (6)$$

$$\dot{\phi}_1 = (\hat{d}^{(1)} \times \dot{\hat{d}}^{(1)}) \cdot \hat{z}, \quad (7)$$

$$\dot{\phi}_2 = (\hat{d}^{(2)} \times \dot{\hat{d}}^{(2)}) \cdot \hat{z}, \quad (8)$$

Here,

$$\dot{\hat{d}}^{(1)} = (\mathcal{I} - \hat{d}^{(1)} \hat{d}^{(1)}) \cdot (\Gamma_1 \mathbf{E}(\mathbf{x}_1) + \mathbf{W}(\mathbf{x}_1)) \cdot \hat{d}^{(1)} \quad (9)$$

$$\dot{\hat{d}}^{(2)} = (\mathcal{I} - \hat{d}^{(2)} \hat{d}^{(2)}) \cdot (\Gamma_2 \mathbf{E}(\mathbf{x}_2) + \mathbf{W}(\mathbf{x}_2)) \cdot \hat{d}^{(2)}, \quad (10)$$

where $\mathbf{E}(\mathbf{x}_\alpha)$ and $\mathbf{W}(\mathbf{x}_\alpha)$ are the rate-of-strain and vorticity tensors evaluated at the position of particle α . These will be given in detail in the next section. We also recall that

$$\mathbf{S}^{(1)} = S_{cc}^{(1)} \hat{c}^{(1)} \hat{c}^{(1)} + S_{dd}^{(1)} \hat{d}^{(1)} \hat{d}^{(1)} + S_{ee}^{(1)} \hat{e}^{(1)} \hat{e}^{(1)}, \quad (11)$$

$$\mathbf{S}^{(2)} = S_{cc}^{(2)} \hat{c}^{(2)} \hat{c}^{(2)} + S_{dd}^{(2)} \hat{d}^{(2)} \hat{d}^{(2)} + S_{ee}^{(2)} \hat{e}^{(2)} \hat{e}^{(2)}. \quad (12)$$

For the in-plane dynamics, we need the \hat{c} , \hat{d} , and \hat{e} vectors expressed in terms of ϕ_1 and ϕ_2 and the Cartesian unit vectors:

$$\hat{c}^{(1)} = -\sin \phi_1 \hat{x} + \cos \phi_1 \hat{y}, \quad (13)$$

$$\hat{d}^{(1)} = \cos \phi_1 \hat{x} + \sin \phi_1 \hat{y}, \quad (14)$$

$$\hat{e}^{(1)} = 0, \quad (15)$$

as well as the corresponding expressions for $\hat{c}^{(2)}$, $\hat{d}^{(2)}$, and $\hat{e}^{(2)}$. We thus obtain

$$\begin{aligned} \mathbf{S}^{(1)} = & S_{cc}^{(1)} [\sin^2 \phi_1 \hat{x}\hat{x} - \sin \phi_1 \cos \phi_1 (\hat{x}\hat{y} + \hat{y}\hat{x}) + \cos^2 \phi_1 \hat{y}\hat{y}] \\ & + S_{dd}^{(1)} [\cos^2 \phi_1 \hat{x}\hat{x} + \sin \phi_1 \cos \phi_1 (\hat{x}\hat{y} + \hat{y}\hat{x}) + \sin^2 \phi_1 \hat{y}\hat{y}], \end{aligned} \quad (16)$$

and the corresponding expression for $\mathbf{S}^{(2)}$. These expressions are convenient for implementation in computer algebra, along with

$$\dot{x} = U_s^{(2)} \cos(\phi_2) - U_s^{(1)} \cos(\phi_1) - \frac{3x (\mathbf{x} \cdot \mathbf{S}^{(1)} \cdot \mathbf{x} + \mathbf{x} \cdot \mathbf{S}^{(2)} \cdot \mathbf{x})}{8\pi\mu(x^2 + y^2)^{5/2}}, \quad (17)$$

$$\dot{y} = U_s^{(2)} \sin(\phi_2) - U_s^{(1)} \sin(\phi_1) - \frac{3y (\mathbf{x} \cdot \mathbf{S}^{(1)} \cdot \mathbf{x} + \mathbf{x} \cdot \mathbf{S}^{(2)} \cdot \mathbf{x})}{8\pi\mu(x^2 + y^2)^{5/2}}. \quad (18)$$

Head-to-head bound state

First, we consider the head-to-head dynamics ($x \neq 0$, $y = 0$, $\phi_1 = 0$, and $\phi_2 = \pi$). By symmetry, $\dot{y} = 0$, $\dot{\phi}_1 = 0$, and $\dot{\phi}_2 = 0$. Moreover, $\vec{x} = x\hat{x}$. It follows that

$$\mathbf{S}^{(1)} = S_{cc}^{(1)}\hat{y}\hat{y} + S_{dd}^{(1)}\hat{x}\hat{x}, \quad (19)$$

$$\mathbf{S}^{(2)} = S_{cc}^{(2)}\hat{y}\hat{y} + S_{dd}^{(2)}\hat{x}\hat{x}, \quad (20)$$

and therefore

$$x_i S_{ij}^{(1)} x_j = x^2 S_{dd}^{(1)}, \quad (21)$$

$$x_i S_{ij}^{(2)} x_j = x^2 S_{dd}^{(2)}. \quad (22)$$

The equation of motion for x becomes

$$\dot{x} = -U_s^{(2)} - U_s^{(1)} - \frac{3(S_{dd}^{(1)} + S_{dd}^{(2)})}{8\pi\mu x^2}. \quad (23)$$

Solving for $\dot{x} = 0$ and $x = d_0$ gives the head-to-head bound state separation

$$d_0 = \sqrt{\frac{-3(S_{dd}^{(1)} + S_{dd}^{(2)})}{8\pi\mu(U_s^{(2)} + U_s^{(1)})}}. \quad (24)$$

Head-to-tail bound state

For a head-to-tail configuration ($x \neq 0$, $y = 0$, $\phi_1 = 0$, and $\phi_2 = 0$), the equation of motion for x is identical, except for the sign of the first term:

$$\dot{x} = U_s^{(2)} - U_s^{(1)} - \frac{3(S_{dd}^{(1)} + S_{dd}^{(2)})}{8\pi\mu x^2}. \quad (25)$$

We therefore obtain

$$d_0 = \sqrt{\frac{3(S_{dd}^{(1)} + S_{dd}^{(2)})}{8\pi\mu(U_s^{(2)} - U_s^{(1)})}}. \quad (26)$$

Both particles move with the same steady velocity. We can obtain the velocity U of the pair by calculating the velocity of particle 1:

$$U = U_s^{(1)} + \frac{3S_{dd}^{(2)}}{8\pi\mu d_0^2}, \quad (27)$$

$$U = U_s^{(1)} + \frac{S_{dd}^{(2)}(U_s^{(2)} - U_s^{(1)})}{S_{dd}^{(1)} + S_{dd}^{(2)}}. \quad (28)$$

MINIMAL MODEL: LINEAR STABILITY ANALYSIS

The linear stability of a bound state (i.e., fixed point) can be determined from the eigenvalues of the Jacobian. For a fixed point, the Jacobian is constructed as follows:

$$\mathbf{J} = \begin{pmatrix} \frac{\partial \dot{x}}{\partial x} & \frac{\partial \dot{x}}{\partial y} & \frac{\partial \dot{x}}{\partial \phi_1} & \frac{\partial \dot{x}}{\partial \phi_2} \\ \frac{\partial \dot{y}}{\partial x} & \frac{\partial \dot{y}}{\partial y} & \frac{\partial \dot{y}}{\partial \phi_1} & \frac{\partial \dot{y}}{\partial \phi_2} \\ \frac{\partial \dot{\phi}_1}{\partial x} & \frac{\partial \dot{\phi}_1}{\partial y} & \frac{\partial \dot{\phi}_1}{\partial \phi_1} & \frac{\partial \dot{\phi}_1}{\partial \phi_2} \\ \frac{\partial \dot{\phi}_2}{\partial x} & \frac{\partial \dot{\phi}_2}{\partial y} & \frac{\partial \dot{\phi}_2}{\partial \phi_1} & \frac{\partial \dot{\phi}_2}{\partial \phi_2} \end{pmatrix}_{x=d_0, y=0, \phi_1=0, \phi_2=0 \text{ or } \phi_2=\pi} \quad (29)$$

where the choice of $\phi_2 = 0$ or $\phi_2 = \pi$ corresponds to a head-to-tail or head-to-head configuration, respectively. The Jacobian can be obtained numerically, by approximating the partial derivatives using finite differences, or analytically.

At this point, it is necessary to specify $\mathbf{E}(\mathbf{x}_\alpha)$ and $\mathbf{W}(\mathbf{x}_\alpha)$ as functions of x , y , ϕ_1 , and ϕ_2 .

The rate-of-strain and vorticity tensors can be constructed from the fluid velocity field:

$$\mathbf{E} = \frac{1}{2} (\nabla \mathbf{u} + \nabla \mathbf{u}^T), \quad (30)$$

$$\mathbf{W} = \frac{1}{2} (\nabla \mathbf{u} - \nabla \mathbf{u}^T). \quad (31)$$

Using $\text{tr}(\mathbf{S}) = 0$ and Eq. 4 in the main text, one can obtain the following partial derivative of the velocity field due to a stresslet located at the origin:

$$\frac{\partial u_i}{\partial x_\ell} = \frac{1}{8\pi\mu r^5} \left(-3x_j x_k \delta_{i\ell} S_{jk} - 3x_i x_k S_{\ell k} - 3x_i x_j S_{j\ell} + \frac{15x_i x_j x_k x_\ell S_{jk}}{r^2} \right). \quad (32)$$

Using $S_{j\ell} = S_{\ell j}$, we can combine the second and third terms in the parentheses:

$$\frac{\partial u_i}{\partial x_\ell} = \frac{1}{8\pi\mu r^5} \left(-3x_j x_k \delta_{i\ell} S_{jk} - 6x_i x_k S_{\ell k} + \frac{15x_i x_j x_k x_\ell S_{jk}}{r^2} \right). \quad (33)$$

The rate-of-strain tensor is

$$E_{i\ell} = \frac{1}{8\pi\mu r^5} \left(-3x_j x_k \delta_{i\ell} S_{jk} - 3x_i x_k S_{\ell k} - 3x_\ell x_k S_{ik} + \frac{15x_i x_j x_k x_\ell S_{jk}}{r^2} \right). \quad (34)$$

For implementation in computer algebra, it is convenient to express this quantity in vector notation:

$$\mathbf{E} = \frac{1}{8\pi\mu r^5} \left(-3\mathcal{I}(\mathbf{x} \cdot \mathbf{S} \cdot \mathbf{x}) - 3\mathbf{x}(\mathbf{S} \cdot \mathbf{x}) - 3(\mathbf{S} \cdot \mathbf{x})\mathbf{x} + \frac{15(\mathbf{x} \cdot \mathbf{S} \cdot \mathbf{x})\mathbf{xx}}{r^2} \right). \quad (35)$$

Concerning the vorticity tensor W_{ij} , it is important to note that we are using the convention $(\nabla \mathbf{u})_{ij} \equiv \frac{\partial u_i}{\partial x_j}$. Thus, $W_{ij} = \frac{1}{2} \left(\frac{\partial u_i}{\partial x_j} - \frac{\partial u_j}{\partial x_i} \right)$. Since the vorticity tensor is anti-symmetric, its sign is sensitive to the choice of convention. (The consistency of this convention with the Jeffery equation as given in Eq. 2 of the main text can be checked by noting that the vorticity contribution $(\mathcal{I} - \hat{d}^{(\alpha)} \hat{d}^{(\alpha)}) \cdot \mathbf{W} \cdot \hat{d}^{(\alpha)}$ should give a contribution identical to $\frac{1}{2} \boldsymbol{\omega} \times \hat{d}^{(\alpha)}$, where $\boldsymbol{\omega} = \nabla \times \mathbf{u}$.) We obtain

$$W_{i\ell} = \frac{3}{8\pi\mu r^5} (-x_i x_k S_{\ell k} + x_\ell x_k S_{ik}), \quad (36)$$

or

$$\mathbf{W} = \frac{3}{8\pi\mu r^5} (-\mathbf{x} (\mathbf{S} \cdot \mathbf{x}) + (\mathbf{S} \cdot \mathbf{x}) \mathbf{x}). \quad (37)$$

We note that only even numbers of factors of \mathbf{x} appear in each term in Eq. 35 and Eq. 37. Therefore, no sign inversion is needed to use these expressions to find the flow components at particle 1 induced by particle 2. This results from the nematic symmetry of the stresslet. It follows that

$$\mathbf{E}(\mathbf{x}_1) = \frac{1}{8\pi\mu d^5} \left(-3\mathcal{I} (\mathbf{x} \cdot \mathbf{S}^{(2)} \cdot \mathbf{x}) - 3\mathbf{x} (\mathbf{S}^{(2)} \cdot \mathbf{x}) - 3(\mathbf{S}^{(2)} \cdot \mathbf{x}) \mathbf{x} + \frac{15(\mathbf{x} \cdot \mathbf{S}^{(2)} \cdot \mathbf{x}) \mathbf{xx}}{d^2} \right), \quad (38)$$

$$\mathbf{W}(\mathbf{x}_1) = \frac{3}{8\pi\mu d^5} (-\mathbf{x} (\mathbf{S}^{(2)} \cdot \mathbf{x}) + (\mathbf{S}^{(2)} \cdot \mathbf{x}) \mathbf{x}), \quad (39)$$

and corresponding expressions for particle 2, where \mathbf{x} is again the vector from particle 1 to particle 2, and $d = |\mathbf{x}| = \sqrt{x^2 + y^2}$.

Head-to-head bound state

From the governing dynamical system, we analytically (with computer algebra) obtain the Jacobian

$$\mathbf{J} = \begin{pmatrix} \frac{3(S_{dd}^{(1)} + S_{dd}^{(2)})}{4\pi\mu d_0^3} & 0 & 0 & 0 \\ 0 & -\frac{3(S_{dd}^{(1)} + S_{dd}^{(2)})}{8\pi\mu d_0^3} & -U_s^{(1)} & -U_s^{(2)} \\ 0 & -\frac{3(S_{dd}^{(2)}(1-4\Gamma_1) + S_{cc}^{(2)}(-1+\Gamma_1))}{8\pi\mu d_0^4} & -\frac{9S_{dd}^{(2)}\Gamma_1}{8\pi\mu d_0^3} & \frac{3(S_{cc}^{(2)} - S_{dd}^{(2)})(-1+\Gamma_1)}{8\pi\mu d_0^3} \\ 0 & -\frac{3(S_{dd}^{(1)}(1-4\Gamma_2) + S_{cc}^{(1)}(-1+\Gamma_2))}{8\pi\mu d_0^4} & \frac{3(S_{cc}^{(1)} - S_{dd}^{(1)})(-1+\Gamma_2)}{8\pi\mu d_0^3} & -\frac{9S_{dd}^{(1)}\Gamma_2}{8\pi\mu d_0^3} \end{pmatrix}. \quad (40)$$

From the zeroes in the first row and first column, we note that translations in the x direction decouple from translations in y and rotations. By inspection, we immediately obtain the

first requirement for stability: $(S_{dd}^{(1)} + S_{dd}^{(2)}) < 0$. This is the “net pusher” requirement. Next, we consider the densely populated 3x3 submatrix obtained by removing the first row and first column of \mathbf{J} . The characteristic equation of this submatrix is:

$$\lambda^3 + A\lambda^2 + B\lambda = 0, \quad (41)$$

with

$$A = \frac{3(S_{dd}^{(1)} + S_{dd}^{(2)}) + 9S_{dd}^{(2)}\Gamma_1 + 9S_{dd}^{(1)}\Gamma_2}{8\pi\mu d_0^3} \quad (42)$$

and

$$B = \frac{-3U_s^{(1)}(S_{dd}^{(2)}(1 - 4\Gamma_1) + S_{cc}^{(2)}(-1 + \Gamma_1)) - 3U_s^{(2)}(S_{dd}^{(1)}(1 - 4\Gamma_2) + S_{cc}^{(1)}(-1 + \Gamma_2))}{8\pi\mu d_0^4} + \frac{27(S_{dd}^{(2)}\Gamma_1 + S_{dd}^{(1)}\Gamma_2)(S_{dd}^{(1)} + S_{dd}^{(2)}) + 81S_{dd}^{(1)}S_{dd}^{(2)}\Gamma_1\Gamma_2 - 9(S_{cc}^{(1)} - S_{dd}^{(1)})(S_{cc}^{(2)} - S_{dd}^{(2)})(-1 + \Gamma_1)(-1 + \Gamma_2)}{64\pi^2\mu^2 d_0^6}. \quad (43)$$

It is immediately apparent that one of the eigenvalues is $\lambda = 0$. This is to be expected, since, for convenience, we considered more coordinates (four) than was needed to specify the state of the system (three). The $\lambda = 0$ eigenvalue therefore corresponds to a symmetry of the dynamical system. Factoring out this eigenvalue, we obtain

$$\lambda^2 + A\lambda + B = 0. \quad (44)$$

Although we could solve for λ , we instead apply the Routh-Hurwitz stability criterion to determine the two remaining requirements for dynamical stability. For a quadratic characteristic equation, the Routh-Hurwitz criterion specifies that a necessary and sufficient condition for stability is that all coefficients of the equation are positive. In other words, we require $A > 0$ and $B > 0$. The requirement on A gives

$$(S_{dd}^{(1)} + S_{dd}^{(2)}) + 3(S_{dd}^{(2)}\Gamma_1 + S_{dd}^{(1)}\Gamma_2) > 0. \quad (45)$$

For a pair of identical particles, the requirement $A > 0$ reduces to $\Gamma < -1/3$, and the requirement $B > 0$ reduces to $[S_{cc}(-1 + \Gamma) + S_{dd}(1 + 2\Gamma)][S_{cc}(-1 + \Gamma) - S_{dd}(1 + 4\Gamma)] < 0$. For a pair of identical *axisymmetric* squirmers, the requirement $B > 0$ further reduces to $(1 + \Gamma)(1 + 9\Gamma) > 0$. Given that $-1 < \Gamma < 1$ by definition, this requirement finally reduces to $\Gamma > -1/9$. Thus, for axisymmetric squirmers, we obtain incompatible requirements.

Head-to-tail bound state

The Jacobian matrix for the head-to-tail bound state is identical to the Jacobian for the head-to-head bound state, except that the entry in the second row, fourth column in $U_s^{(2)}$. Thus, the first requirement for stability is again $(S_{dd}^{(1)} + S_{dd}^{(2)}) < 0$, i.e., the pair is a “net pusher.” As before, the characteristic equation reduces to Eq. 44. Moreover, the coefficient A is again

$$A = \frac{3(S_{dd}^{(1)} + S_{dd}^{(2)}) + 9S_{dd}^{(2)}\Gamma_1 + 9S_{dd}^{(1)}\Gamma_2}{8\pi\mu d_0^3}, \quad (46)$$

giving the condition

$$(S_{dd}^{(1)} + S_{dd}^{(2)}) + 3(S_{dd}^{(2)}\Gamma_1 + S_{dd}^{(1)}\Gamma_2) > 0. \quad (47)$$

The coefficient B is nearly identical to Eq. 43, but differs in the sign of the second term in the numerator of the fraction with d^4 in the denominator:

$$B = \frac{-3U_s^{(1)}(S_{dd}^{(2)}(1 - 4\Gamma_1) + S_{cc}^{(2)}(-1 + \Gamma_1)) + 3U_s^{(2)}(S_{dd}^{(1)}(1 - 4\Gamma_2) + S_{cc}^{(1)}(-1 + \Gamma_2))}{8\pi\mu d_0^4} + \frac{27(S_{dd}^{(2)}\Gamma_1 + S_{dd}^{(1)}\Gamma_2)(S_{dd}^{(1)} + S_{dd}^{(2)}) + 81S_{dd}^{(1)}S_{dd}^{(2)}\Gamma_1\Gamma_2 - 9(S_{cc}^{(1)} - S_{dd}^{(1)})(S_{cc}^{(2)} - S_{dd}^{(2)})(-1 + \Gamma_1)(-1 + \Gamma_2)}{64\pi^2\mu^2 d_0^6}. \quad (48)$$

We recall that the second condition for stability is $B > 0$.

Head-to-tail bound states of axisymmetric squirmers.

For non-identical *axisymmetric* squirmers, the condition $A > 0$ becomes

$$\sigma_0^{(1)} + \sigma_0^{(2)} + 3(\sigma_0^{(2)}\Gamma_1 + \sigma_0^{(1)}\Gamma_2) > 0. \quad (49)$$

The condition $B > 0$ becomes, using the “net pusher” criterion $\sigma_0^{(1)} + \sigma_0^{(2)} < 0$,

$$\begin{aligned} & \left(-2(\Gamma_2 - 1)\sigma_1^2 + (\Gamma_2 + \Gamma_1(9\Gamma_2 + 7) - 1)\sigma_0^{(2)}\sigma_0^{(1)} + 4\Gamma_1\sigma_0^{(2)^2} \right) U_s^{(2)} \\ & - \left(\Gamma_2\sigma_0^{(1)} \left((9\Gamma_1 + 7)\sigma_0^{(2)} + 4\sigma_0^{(1)} \right) + (\Gamma_1 - 1)\sigma_0^{(2)} \left(\sigma_0^{(1)} - 2\sigma_0^{(2)} \right) \right) U_s^{(1)} < 0. \end{aligned} \quad (50)$$

Defining the parameters $S \equiv \sigma_0^{(2)}/\sigma_0^{(1)}$ and $V \equiv U_s^2/U_s^1$, with $V \geq 0$, we obtain

$$\text{sgn} \left(\sigma_0^{(1)} \right) [1 + S + 3(S\Gamma_1 + \Gamma_2)] > 0 \quad (51)$$

and

$$\begin{aligned} \Gamma_2((S-2)V - 7S - 4) + \Gamma_1 S(4SV + 2S + 9\Gamma_2(V-1) + 7V - 1) \\ - S(2S + V - 1) + 2V < 0. \end{aligned} \quad (52)$$

In addition, the “net pusher” criterion can be expressed in term of S :

$$\text{sgn}\left(\sigma_0^{(1)}\right)(1+S) < 0. \quad (53)$$

These expressions make clear that the phase boundary exists in a space defined by four parameters: Γ_1 , Γ_2 , S , and V .

It is instructive to fix Γ_1 , Γ_2 , and $\text{sgn}\left(\sigma_0^{(1)}\right)$, and consider the two-dimensional phase subspace defined by V and S . First, we note that Eqs. 51 and 53 do not involve V , and place numerical bounds on S . Then, considering Eq. 52, we note that it can be written in the form

$$f_1(S) + f_2(S)V < 0, \quad (54)$$

where $f_1(S)$ and $f_2(S)$ are functions of S . Depending on the numerical bounds on S , satisfaction of the condition given in Eq. 54 may or may not depend on the value of V . As a concrete example, we consider $\text{sgn}\left(\sigma_0^{(1)}\right) = -1$, $\Gamma_1 = -0.7$, and $\Gamma_2 = 0.2$. From Eq. 53, we obtain $S > -1$. From Eq. 51, we obtain a stricter lower bound, $S > 1.46$. Eq. 52 gives $(-0.8 + 1.56S - 3.4S^2) + (1.6 - 6.96S - 2.8S^2)V < 0$. Both terms in parentheses are negative for $S > 1.46$. Therefore, the condition is satisfied for all $V > 0$, and the phase boundary reduces to a line $S = 1.46$ in (V, S) space.

A no-cargo theorem for far-field bound states.

Using active colloids as “cargo carriers” is often suggested as a desirable potential application in lab-on-a-chip systems. In the framework of our far-field theory, we now show that it is not possible to have a stable collinear bound state in which one of the particles is an inert cargo with no self-propulsion and no active stresslet. First, given the criterion $U_s^{(1)} > U_s^{(2)}$, it is clear that the trailing particle cannot be an inert cargo. Now we consider the possibility that particle 2 is inert, i.e., that $U_s^{(2)} = 0$, $S_{cc}^{(2)} = 0$, $S_{dd}^{(2)} = 0$, and $S_{ee}^{(2)} = 0$. Eq. 47 gives:

$$S_{dd}^{(1)}(1 + 3\Gamma_2) > 0. \quad (55)$$

Since the pair must be a net squirmer, $S_{dd}^{(1)} < 0$, so that $\Gamma_2 < -1/3$. Similarly, using $S_{dd}^{(1)} < 0$, the criterion $B > 0$ yields $\Gamma_2 > 0$. We therefore obtain a contradiction. We note

that this result does not exclude the possibility of “cargo-carrying” sustained by near-field hydrodynamics or lubrication forces, particle or fluid inertia, phoretic/chemical interactions, or other effects not included in our minimal theory.

PROPERTIES OF THE STRESSLET TENSOR

Eq. 6 in the main text is generic because the stresslet tensor is symmetric and real-valued. Thus, the principal axes are orthogonal, and one can always rotate to a frame in which the stresslet tensor is diagonal.

However, we note some technical caveats. First, the particle’s propulsion velocity may or may not be aligned with one of the principal axes. Subsequent to Eq. 6 in the main text, we assume that the propulsion velocity is aligned with a principal axis \hat{d} . Secondly, the principal axes may or may not be aligned with axes of a Cartesian coordinate system that naturally corresponds to a confining geometry. We can give an example in which both of these complications occur. We consider a discoidal ICEP particle near a solid planar wall, as in Katuri *et al.* [?] The AC field is oriented normal to the wall. The particle’s axis of (geometric and material) symmetry is oriented parallel to the wall, and the particle center has height h above the wall. As the most natural coordinate system for the “laboratory” frame, we define the z -direction as being aligned with the wall normal, and the x - and y -directions to lie in the plane of the wall. In this frame, we numerically calculate, using Eq. 1 in the main text and theoretical methods in Katuri *et al.*, that the stresslet tensor is not diagonal. (Two off-diagonal elements are roughly 3x smaller in magnitude than the smallest magnitude element on the diagonal.) Additionally, we find that the particle velocity vector is not aligned with a principal axis of the stresslet. However, when the particle is far from the wall (h is large), the off-diagonal components of the stresslet tensor diminish, and the particle’s direction of propulsion is nearly aligned with one of the principal axes. Thus, the analysis in the present work is a good approximation for ICEP particles in free space. It would be relatively straightforward to extend the analysis to accommodate the effects mentioned above. This could be considered in future work that is oriented towards application to ICEP particles moving near a planar substrate. In the present case, these technicalities are not considered in order to maintain a simple and clear presentation.

SPHEROIDAL COORDINATE SYSTEMS

To test our analytical predictions, we compare the results to numeric calculations with the boundary element method. In its implementation, we use prolate and oblate spheroidal coordinates. In this Section, we refer to the Cartesian coordinate system in Fig. 1 of the main text, but omit the prime symbols for notational clarity. The prolate spheroidal coordinates (τ, ξ, φ) are related to the Cartesian coordinates via the transformation [?]]

$$\begin{aligned} x &= c\sqrt{(\tau^2 - 1)(1 - \xi^2)} \sin(\varphi), \\ y &= c\tau\xi, \\ z &= c\sqrt{(\tau^2 - 1)(1 - \xi^2)} \cos(\varphi), \end{aligned}$$

with the geometric prefactor $c = \sqrt{1 - r_e^2}$ and have basis vectors

$$\begin{aligned} \mathbf{e}_\tau &= \left(\frac{\tau \cdot \sqrt{1 - \xi^2}}{\sqrt{\tau^2 - 1}} \mathbf{e}_z + \xi \mathbf{e}_y \right) \cdot \frac{\sqrt{\tau^2 - 1}}{\sqrt{\tau^2 - \xi^2}}, \\ \mathbf{e}_\xi &= \left(\frac{\xi \cdot \sqrt{\tau^2 - 1}}{\sqrt{1 - \xi^2}} \mathbf{e}_z + \tau \mathbf{e}_y \right) \cdot \frac{\sqrt{1 - \xi^2}}{\sqrt{\tau^2 - \xi^2}} \end{aligned} \quad (56)$$

for $\varphi = 0$. Similarly, the transformations for the oblate spheroidal coordinates (λ, ξ, φ)

$$\begin{aligned} x &= \bar{c}\sqrt{(1 + \lambda^2)(1 - \xi^2)} \sin(\varphi), \\ y &= \bar{c}\lambda\xi, \\ z &= \bar{c}\sqrt{(1 + \lambda^2)(1 - \xi^2)} \cos(\varphi), \end{aligned}$$

use a geometric prefactor $\bar{c} = \sqrt{r_e^2 - 1}$ and have basis vectors

$$\begin{aligned} \mathbf{e}_\lambda &= \left(\frac{\lambda \cdot \sqrt{1 - \xi^2}}{\sqrt{1 + \lambda^2}} \mathbf{e}_z + \xi \mathbf{e}_y \right) \cdot \frac{\sqrt{1 + \lambda^2}}{\sqrt{\lambda^2 + \xi^2}}, \\ \mathbf{e}_\xi &= \left(\frac{-\xi \cdot \sqrt{1 + \lambda^2}}{\sqrt{1 - \xi^2}} \mathbf{e}_z + \lambda \mathbf{e}_y \right) \cdot \frac{\sqrt{1 - \xi^2}}{\sqrt{\lambda^2 + \xi^2}} \end{aligned} \quad (57)$$

for $\varphi = 0$.

VELOCITY AND STRESSLET OF AXISYMMETRIC SPHEROIDAL SQUIRMER

For axisymmetric particles, we follow the spheroidal squirmers model presented in Ref. ? with slip velocities defined by

$$v_s(\xi) = \tau_0(\tau_0^2 - \xi^2)^{-1/2} P_n^1(\xi). \quad (58)$$

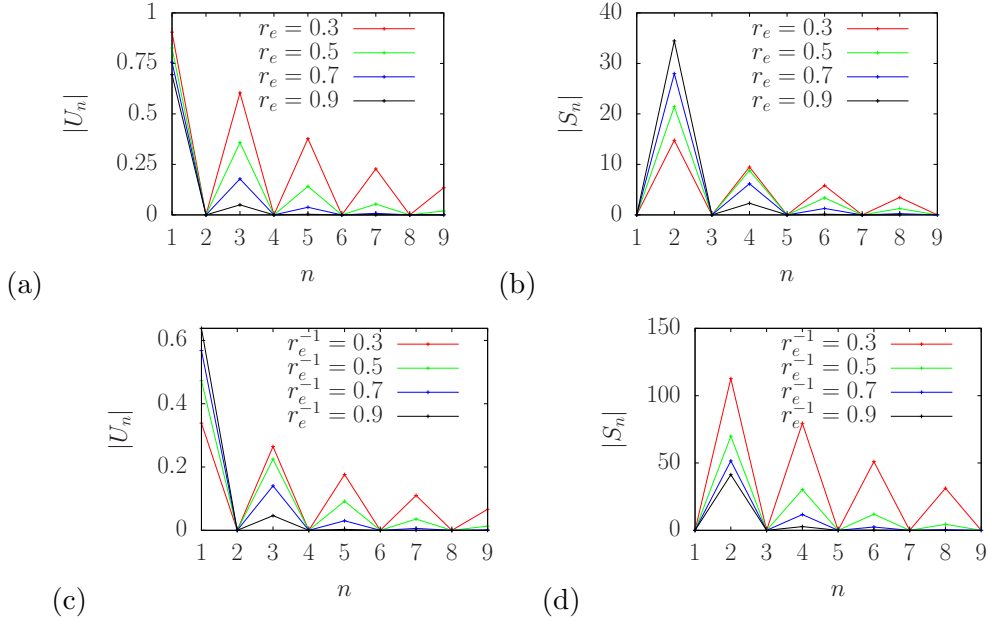


FIG. 2. (a) The absolute value $|U_n|$ of the contribution of the slip modes $n = 1, 3, 5, 7$ to the velocity of a prolate squirmer for aspect ratios $r_e = 0.3, 0.5, 0.7, 0.9$. (b) The absolute value $|S_n|$ of the contribution of the slip modes $n = 1, 3, 5, 7$ to the stresslet of a prolate squirmer for aspect ratios $r_e = 0.3, 0.5, 0.7, 0.9$. (c) The absolute value $|U_n|$ of the contribution of the slip modes $n = 1, 3, 5, 7$ to the velocity of an oblate squirmer for aspect ratios $r_e^{-1} = 0.3, 0.5, 0.7, 0.9$. (d) The absolute value $|S_n|$ of the contribution of the slip modes $n = 1, 3, 5, 7$ to the stresslet of an oblate squirmer for aspect ratios $r_e^{-1} = 0.3, 0.5, 0.7, 0.9$. The lines represent only a guide to the eye.

ξ and τ are spheroidal coordinates. The free space velocity U_s and stresslet $S_0 = \frac{3}{2}\sigma_0$ for each individual particle only depends on its aspect ratio r_e and squirming amplitudes B_n . In Ref. ? , the figures 3, 8 and 9, are affected by typos in the data generating scripts (more details will be available in a forthcoming erratum). The corrected versions are presented here in Fig. 2 (and in the erratum). The qualitative analysis is unaffected by the miscalculations, however it significantly changes the value of the properties. In Fig. 3 we compare the analytic results for the velocity $|U_n|$ and $|S_n|$ induced by B_1 and B_2 squirmer modes to numerical calculations done with BEM. Eq. 3 in the main text is used to calculate the stresslet.

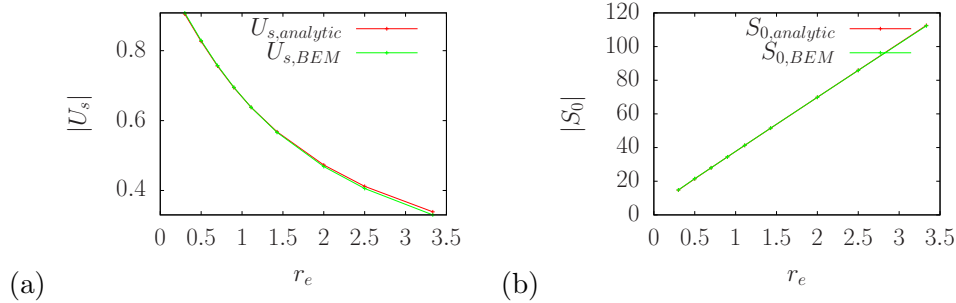


FIG. 3. (a) Comparison between the analytically predicted and the numerically calculated velocity $|U_s|$ over a range of aspect ratios r_e . For these calculations only B_1 is non-zero. (b) Comparison between the analytic predicted and the numerically calculated stresslet $|S|$ over a range of aspect ratios r_e . For these calculations only B_2 is non-zero.

SEPARATION DISTANCE

The second main prediction of our model besides the stability of the pairs is their steady separation distance d_0 . d_0 can even be calculated for two particles which are only stable against perturbations in the direction of propulsion. In Fig. 4 we show how our prediction compares against the distance calculated with the BEM. Similar to the stability analysis in the main text, we generally obtain good agreement between the theory and BEM, especially for the spheres and the prolate particles. For the oblate particles, our analytical prediction are consistently smaller than the results of our numerical calculations, and the relative error becomes more pronounced for small separation distance d_0 between the particles.

INDUCED CHARGE ELECTROPHORESIS

In order to model the interaction of particles with non-axisymmetric actuation, we first consider a single spheroidal Janus particle moving by ICEP in unbounded solution. The particle consists of a dielectric core with a fraction of its surface covered by metal. The metal coverage is axisymmetric, and the particle aspect ratio is defined as above. A uniform electric field $\mathbf{E} = E_0 \hat{z}$ is perpendicular to the particle axis \hat{d} : $\hat{z} = \hat{e}$. In the DC limit, the time-averaged electrostatic potential φ obeys $\nabla^2 \varphi = 0$, as well as the boundary conditions $\hat{n} \cdot \nabla \varphi = 0$ on the surface of the particle, and $\varphi \rightarrow -E_0 z$ as $|\mathbf{x}| \rightarrow \infty$. As described in Refs. ? and ? , the surface slip can be obtained from the surface potential. Turning to the

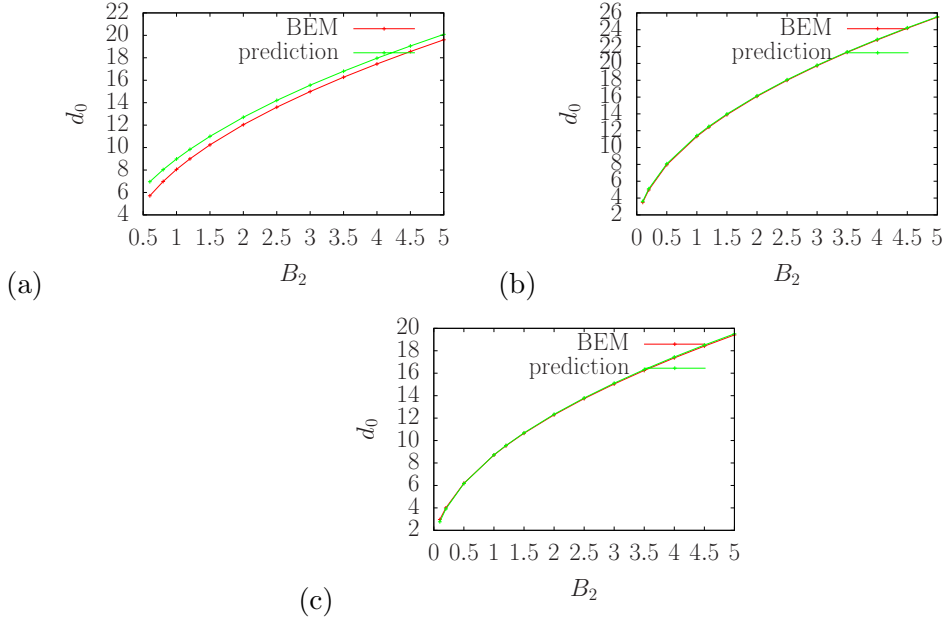


FIG. 4. Comparison between the predicted and the calculated (BEM) separation distance for head-to-tail pairs. The velocities $U_s^{(2)} = 0.2$ and $U_s^{(1)} = 0.25$ are fixed in all cases. We show three different geometries: (a) $r_e^{(1)} = 1.1055$ and $r_e^{(2)} = 3$, (b) $r_e^{(1)} = 1.1055$ and $r_e^{(2)} = 1.1055$, and (c) $r_e^{(1)} = 0.5774$ and $r_e^{(2)} = 0.5774$.

dynamics of interacting pairs, we fix $\mathbf{v}_s^{(\alpha)}$ to be the distribution for an isolated particle, i.e., we neglect electrostatic interactions between particles. Due to the constant surface slip, the particles in this model can be regarded as non-axisymmetric squirmers. The flow obeys the same equations as for the axisymmetric squirmers.

The coverage of a particle by metal is defined by a parameter $\chi_0 \in [1, 1]$. For a spheroid with its center at the origin and its axis of propulsion \hat{d} aligned with the z-axis, regions on the surface of particle with $z \in [-1, \chi_0]$ are taken to be metal, and regions with $z \in (\chi_0, 1]$ are insulating. (Here, as discussed in the main text, the semi-axis of propulsion provides the characteristic length, such that the two poles of the particle are at $z = \pm 1$.) Thus, a particle with $\chi_0 = 0$ has half coverage.

In Fig. 2 in the main text, we plot numerical results for oblate ICEP squirmers using circles. These results were obtained for particles with metal coverage slightly more than half: $\chi_0 = 0.5$. This coverage χ_0 was chosen to obtain a finite gap between particles in a bound state for several values of Γ . For other values of χ_0 , particles tend to “crash” into each other. (We that in Ref. ? , the presence of a nearby bounding surface, i.e., a hard

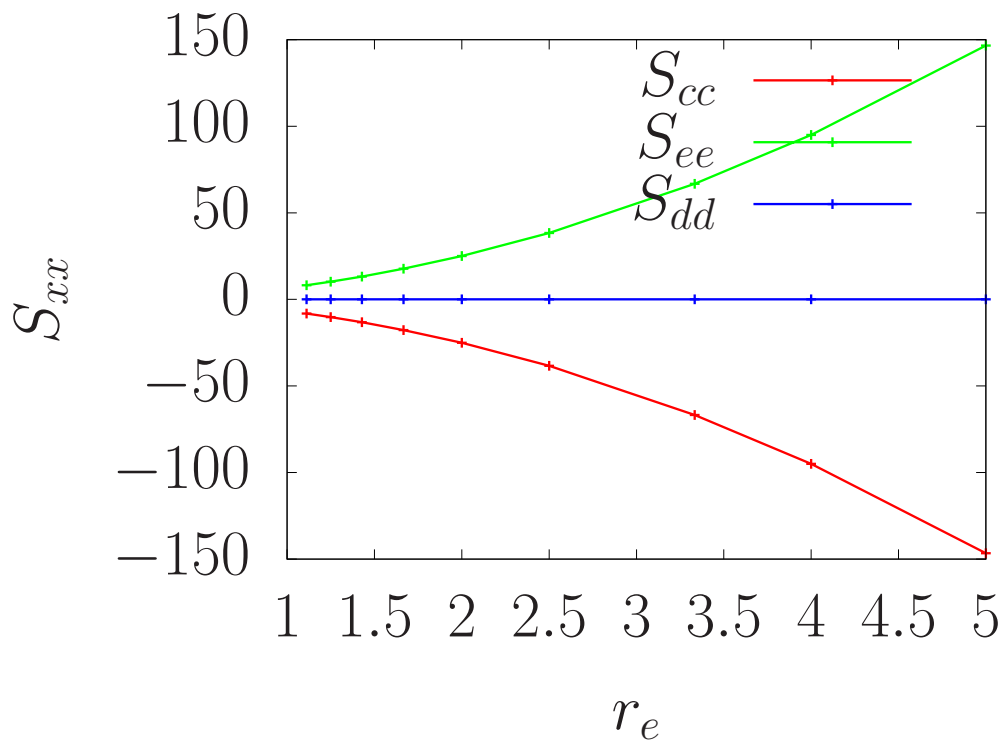


FIG. 5. The S_{dd} , S_{cc} and S_{ee} contributions for a squirmer with constant asymmetric mode $\tilde{B} = 1$ for changing aspect ratio r_e . The lines represent only a guide to the eye.

planar wall, was essential for obtaining bound states of half-covered particles.)

AXISYMMETRIC SQUIRMER MODEL

In Fig. 5 we show the three diagonal components of the stresslet tensor for varying aspect ratio r_e . S_{dd} and U_s are zero for all aspect ratios, and S_{cc} and S_{ee} decrease and increase asymmetrically.